Terahertz radiation as a probe of the dynamics of coherently injected photocurrents in quantum well and graphene systems

Kiran M. Rao* and J. E. Sipe

Department of Physics and Institute for Optical Sciences, University of Toronto, 60 St. George Street, Toronto, Ontario, Canada M5S 1A7

(Received 4 June 2014; revised manuscript received 29 August 2014; published 20 October 2014)

We calculate the terahertz radiation that would be emitted from rotating current densities coherently injected by two-color optical pulses in GaAs and graphene samples in a magnetic field. This is done for realistic experimental geometries and parameters, with scattering and relaxation processes taken into account phenomenologically. Results are presented in the time domain for the expected terahertz signal observed at a detector. We include predictions for bilayer graphene as well as monolayer graphene, and compare with results expected in the absence of a magnetic field.

DOI: 10.1103/PhysRevB.90.155313 PACS number(s): 78.67.Wj, 78.20.Ls, 42.25.Bs, 72.20.Jv

I. INTRODUCTION

Interference between the amplitudes of quantum mechanical pathways can be used to control various properties of matter. This technique of "coherent control" has been applied to a host of atomic, molecular, and condensed matter systems [1–3]. In particular, coherent control has been applied to semiconductor systems to control the direction and magnitude of optically injected photocurrents by adjusting the relative phase parameter of incident laser beams [4–6]. Previously, we investigated theoretically the possibility of the optical control of photocurrents in the presence of an external magnetic field, for GaAs quantum well [7] and graphene [8] systems subject to pulses centered at frequencies ω_0 and $2\omega_0$. For both these systems, we found that interference between one-photon and two-photon excitation pathways could give rise to injected photocurrents of electrons and holes that rotate in time at frequencies determined by the energy differences between the two interfering pathways. This contrasts with the situation in the absence of a magnetic field, where the injected currents are expected to be static after injection, apart from scattering and decay processes.

These injected photocurrents can be experimentally observed by detecting the terahertz radiation emitted during their injection and decay. Such experiments have already been performed on GaAs and graphene systems in the absence of a magnetic field [9,10]. Since the photocurrents are not static when a magnetic field is applied, the terahertz radiation pattern is expected to be qualitatively different from that in the absence of a magnetic field.

The object of the current paper is to calculate explicitly the radiated fields from these photocurrents in the presence of a magnetic field in various excitation and detection scenarios. We present results for three systems: GaAs quantum wells, monolayer graphene, and bilayer (Bernal-stacked) graphene.

In the limit of excitation by pulses that are superpositions of plane waves with fields uniform over the plane of the sample, the calculated injected current density is necessarily uniform in the plane of the quantum well or graphene layer(s), but rotates in time [see Fig. 1(a)]. We showed previously [7] that the optically induced current density in a GaAs quantum well can be written as a sum of contributions from electron and hole charge densities associated with a basis of coherent states, each centered at a particular point in the plane of the material. In this decomposition, as we illustrate in Fig. 1(b), around each point in the sample one can identify a localized electron and hole density, each consisting of a particular superposition of Landau orbitals excited by the optical pulses. The electron density rotates counterclockwise in time about the point in the plane, while the hole density rotates clockwise, with frequencies determined by the energy differences between the two interfering pathways that give rise to these densities. Similar considerations apply to graphene and bilayer graphene.

This decomposition is the natural one to use to extend the calculation to a system subject to exciting pulses that are confined both in time and space; such an extension is necessary to make a realistic calculation of the THz radiation from the system. Since the radii of the Landau orbits involved are far less than the typical distance characterizing the transverse variation of the exciting fields over the sample, we can calculate the current injection at any point from the results of the plane wave calculation, but using the actual values of the electric fields present at that point. The associated electron and hole charge densities induced can then be used to calculate the various multipole moments associated with that point. Since the size of the Landau orbits is also far less than the wavelength of the THz radiation emitted, we can then use these multipole moments to determine the radiation pattern. This is the strategy we adopt in this paper. Not surprisingly, the electric dipole moment is by far the dominant multipole moment, and this is the only one we need to consider.

This paper is structured as follows. In Sec. II we provide general expressions for the optically induced electric dipole moments in the sample. Expressions for the radiated electric field are presented in Sec. III, and we use previous results to calculate the dipole moments specific to GaAs quantum wells and mono- and bilayer graphene in Sec. IV; even in the limit of plane wave excitation, the optical injection of currents in bilayer graphene in a magnetic field has not been presented before. Numerical results for the detected fields are given in Sec. V, and we conclude in Sec. VI.

*krao@physics.utoronto.ca

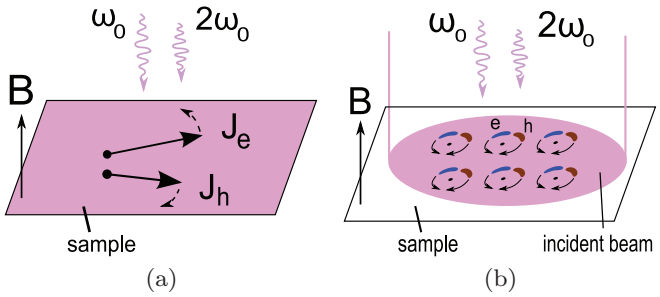

FIG. 1. (Color online) (a) Illustration of rotation of electron (e) and hole (h) current densities in a uniform optical field. (b) Illustration of electron and hole densities about points in the sample, injected by a pulse finite in space and time; the charges rotate about the points as shown.

II. INDUCED DIPOLE MOMENTS

In this section we calculate the electric dipole moments produced by the optical field by considering the optically induced charge density distributions. The system under consideration is in a static, uniform magnetic field directed perpendicular to the plane of the sample. We begin by taking the optical field to be normally incident and uniform over the plane of the sample, with a Gaussian dependence in frequency and thus in time,

$$\mathbf{E}(t) = \int_0^\infty \frac{d\omega}{2\pi}\left[\boldsymbol{\mathcal{E}}_{\omega_0} e^{-(\omega-\omega_0)^2/\Delta_1^2} + \boldsymbol{\mathcal{E}}_{2\omega_0} e^{-(\omega-2\omega_0)^2/\Delta_2^2}\right] e^{-i\omega t} + \text{c.c.} \tag{1}$$

We assume that the pulses extend over many optical periods, so $\Delta_1 \ll \omega_0$ and $\Delta_2 \ll 2\omega_0$. The expression (1) can be identified with the field at the sample position $z = z_0$, with the sample taken to lie in the (xy) plane. Of course, whether the system is a semiconductor quantum well, graphene, or bilayer graphene, there is some extension of the sample in the z direction, but such distances are so small compared to the wavelengths of light involved that the spatial variation in z can be neglected. Previously [7] we calculated, to second order in the optical field, expressions for the amplitudes of exciton states $|CV\rangle$ in a GaAs quantum well and in a graphene monolayer [7], where C and V represent the conduction and valence states that form the exciton, and each comprise a set of quantum numbers, as described in Sec. IV. For any of the systems we consider here, among these quantum numbers are two numbers n and l associated with the wave functions of a two-dimensional electron in a uniform magnetic field perpendicular to the plane (Landau levels) [11], which appear here as envelope functions modulating the periodic functions associated with the lattice [7,8]. The Landau levels are degenerate in l, and for any particular choice of the other quantum numbers we can construct in the l subspace a new (overcomplete) basis of coherent states, each of which is spatially localized around a point in the plane [11].

For the present consideration of an optical field uniform over the plane of the sample, we can focus our attention only on the states centered at the origin, as the states at other locations will behave identically. The coherent state centered at the origin is the same as the state in the l basis with $l = 0$, and so the state centered at the origin and having its other quantum numbers identical with those of C or V can be identified by c or v, where the latter states are identical to the former but with $l = 0$. Focusing only on these localized exciton states $|cv\rangle$, we can identify the time derivatives of the amplitudes of these states from our earlier studies [7,8],

$$\dot{c}_{cv}^{(j)}(t) = -i\omega_{cv} c_{cv}^{(j)}(t) + f^{(j)}(t), \tag{2}$$

where $\omega_{cv} \equiv \omega_c - \omega_v$, and $f^{(1)}(t)$ and $f^{(2)}(t)$ can be considered as driving terms leading to the growth of the amplitude of the state $|cv\rangle$. The first-order coefficient ($j = 1$) represents a one-photon excitation process by a single photon at frequency ω_0 or $2\omega_0$, as represented by the forcing term $f^{(1)}(t)$ which is dependent on the peak amplitudes of the ω_0 and $2\omega_0$ pulses, while the second-order coefficient ($j = 2$) represents a two-photon excitation process by two photons each at frequency ω_0, or by one photon at ω_0 and one photon at $2\omega_0$, as represented by the forcing term $f^{(2)}(t)$, which is also dependent on the amplitudes of the pulses. In order to take into account scattering and dephasing, we can introduce a phenomenological decay time τ_{cv} into (2):

$$\dot{c}_{cv}^{(j)}(t) = -i\omega_{cv} c_{cv}^{(j)}(t) - \frac{1}{\tau_{cv}} c_{cv}^{(j)}(t) + f^{(j)}(t). \tag{3}$$

Solving this equation using the explicit expressions for $f^{(j)}(t)$ we find

$$c_{cv}^{(j)}(t) = \left[\Lambda_{cv}^{(j)} T_{cv}^{(j)}(t) + \Gamma_{cv}^{(j)} U_{cv}^{(j)}(t)\right] e^{-i\omega_{cv}t} e^{-t/\tau_{cv}}, \tag{4}$$

where

$$T_{cv}^{(j)}(t) = \int_{-\infty}^{t} dt' \exp\left(-\gamma_{(j)}^2 t'^2\right) e^{t'/\tau_{cv}} e^{i(\omega_{cv}-2\omega_0)t'},$$

$$U_{cv}^{(j)}(t) = \int_{-\infty}^{t} dt' \exp\left(-\varepsilon_{(j)}^2 t'^2\right) e^{t'/\tau_{cv}} e^{i(\omega_{cv}-\omega_0)t'},$$

with $\gamma_{(1)}^2 \equiv \Delta_2^2/4$, $\gamma_{(2)}^2 \equiv \Delta_1^2/2$, $\varepsilon_{(1)}^2 \equiv \Delta_1^2/4$, $\varepsilon_{(2)}^2 \equiv (\Delta_1^2 + \Delta_2^2)/4$; and

$$\Lambda_{cv}^{(1)} = \frac{e}{4\sqrt{\pi}\hbar}\frac{\Delta_2}{\omega_0}\left(\boldsymbol{\mathcal{E}}_{2\omega_0}\cdot\mathbf{v}_{cv}\right), \tag{5}$$

$$\Gamma_{cv}^{(1)} = \frac{e}{2\sqrt{\pi}\hbar}\frac{\Delta_1}{\omega_0}\left(\boldsymbol{\mathcal{E}}_{\omega_0}\cdot\mathbf{v}_{cv}\right), \tag{6}$$

$$\Lambda_{cv}^{(2)} = \frac{e^2\Delta_1^2}{4\pi i\hbar^2\omega_0^2}\left[\sum_{c'}\frac{\left(\mathbf{v}_{cc'}\cdot\boldsymbol{\mathcal{E}}_{\omega_0}\right)\left(\mathbf{v}_{c'v}\cdot\boldsymbol{\mathcal{E}}_{\omega_0}\right)}{\omega_{c'v}-\omega_0} - \sum_{v'}\frac{\left(\mathbf{v}_{cv'}\cdot\boldsymbol{\mathcal{E}}_{\omega_0}\right)\left(\mathbf{v}_{v'v}\cdot\boldsymbol{\mathcal{E}}_{\omega_0}\right)}{\omega_{cv'}-\omega_0}\right], \tag{7}$$

$$\Gamma_{cv}^{(2)} = -\frac{e^2\Delta_1\Delta_2}{8\pi i\hbar^2\omega_0^2}\left[\sum_{c'}\frac{\left(\mathbf{v}_{cc'}\cdot\boldsymbol{\mathcal{E}}_{2\omega_0}\right)\left(\mathbf{v}_{c'v}\cdot\boldsymbol{\mathcal{E}}^*_{\omega_0}\right)}{\omega_{c'v}+\omega_0} - \sum_{v'}\frac{\left(\mathbf{v}_{cv'}\cdot\boldsymbol{\mathcal{E}}^*_{\omega_0}\right)\left(\mathbf{v}_{v'v}\cdot\boldsymbol{\mathcal{E}}_{2\omega_0}\right)}{\omega_{cv'}+\omega_0} + \sum_{c'}\frac{\left(\mathbf{v}_{cc'}\cdot\boldsymbol{\mathcal{E}}^*_{\omega_0}\right)\left(\mathbf{v}_{c'v}\cdot\boldsymbol{\mathcal{E}}_{2\omega_0}\right)}{\omega_{c'v}-2\omega_0} - \sum_{v'}\frac{\left(\mathbf{v}_{cv'}\cdot\boldsymbol{\mathcal{E}}_{2\omega_0}\right)\left(\mathbf{v}_{v'v}\cdot\boldsymbol{\mathcal{E}}^*_{\omega_0}\right)}{\omega_{cv'}-2\omega_0}\right], \tag{8}$$

with $\mathbf{v}_{cv}$, etc., denoting the matrix elements of the velocity operator between the indicated states. The functions $T_{cv}^{(j)}$ and $U_{cv}^{(j)}$ encapsulate the time dependence of the exciting pulses and the resulting buildup of amplitude in the excited states; the quantities $\Lambda_{cv}^{(j)}$ and $\Gamma_{cv}^{(j)}$ encapsulate the selection rules for one- and two-photon transitions in the relevant system, as discussed earlier [7,8].

We now generalize these results to optical pulses that are confined both in time and space. We assume that the transverse widths of the pulses are much larger than the wavelengths that appear in them with significant amplitudes. Then to good approximation we can identify the field $\mathbf{E}(\mathbf{R},t)$ in the plane of the sample, where $\mathbf{R} = (x,y)$, by multiplying the $\mathcal{E}_{\omega_o}$ and $\mathcal{E}_{2\omega_o}$ appearing in (1) by optical envelope functions that depend on $\mathbf{R}$. We assume that these functions are Gaussian, although that could be easily generalized. Then the ω_0-pulse amplitude $\mathcal{E}_{\omega_o}$ in (1) is replaced by $\mathcal{E}_{\omega_o}[L_1(\mathbf{R})] \equiv \mathcal{E}_{\omega_o}\exp(-R^2/R_1^2)$, and the $2\omega_0$-pulse amplitude $\mathcal{E}_{2\omega_o}$ by $\mathcal{E}_{2\omega_o}[L_2(\mathbf{R})] \equiv \mathcal{E}_{2\omega_o}\exp(-R^2/R_2^2)$, where $R = |\mathbf{R}|$ and R_1 and R_2 specify the transverse extent of the two pulses. Since both R_1 and R_2 will be much larger than the radii of the Landau orbits involved, for the magnetic fields we consider, we can assume that a localized state centered at a particular point $\mathbf{R}$ in the plane experiences a spatially uniform field over its extent, but that states centered at different points experience different fields according to where they are located. Thus the excitation amplitude into the exciton state at $\mathbf{R}$ having the quantum numbers of $|cv\rangle$ can be written in terms of the amplitude in a uniform field, as calculated above, modulated by the appropriate spatial function:

$$d_{cv}(\mathbf{R},t) = e^{-i\omega_{cv}t}e^{-t/\tau_{cv}}\big[\Lambda_{cv}^{(1)}T_{cv}^{(1)}(t)L_2(\mathbf{R}) + \Gamma_{cv}^{(1)}U_{cv}^{(1)}(t)L_1(\mathbf{R}) + \Lambda_{cv}^{(2)}T_{cv}^{(2)}(t)[L_1(\mathbf{R})]^2 + \Gamma_{cv}^{(2)}U_{cv}^{(2)}(t)L_1(\mathbf{R})L_2(\mathbf{R})\big]. \tag{9}$$

We look next at the electron and hole charge densities associated with each point $\mathbf{R}$. In our earlier work [7] these were calculated for the case of a uniform excitation field, and were therefore independent of $\mathbf{R}$. For the present situation of a nonuniform field, they are modified by the spatial dependence that $d_{cv}(\mathbf{R},t)$ has acquired and take the form

$$\rho_{\mathbf{R}}^{e}(\mathbf{r}_e,t) = e\sum_{cc'v} d_{cv}(\mathbf{R},t)d_{c'v}^{*}(\mathbf{R},t)\Psi_{c',\mathbf{R}}^{\dagger}(\mathbf{r}_e)\Psi_{c,\mathbf{R}}(\mathbf{r}_e), \tag{10}$$

$$\rho_{\mathbf{R}}^{h}(\mathbf{r}_h,t) = -e\sum_{cvv'} d_{cv}(\mathbf{R},t)d_{cv'}^{*}(\mathbf{R},t)\Psi_{v,\mathbf{R}}^{\dagger}(\mathbf{r}_h)\Psi_{v',\mathbf{R}}(\mathbf{r}_h), \tag{11}$$

where $e < 0$, and $\Psi_{n,\mathbf{R}}$ is the envelope function associated with the state n centered at position $\mathbf{R}$. It is a one-component function in the case of a GaAs quantum well (within our model), a two-component function for a graphene monolayer, and a four-component function for a graphene bilayer.

The polarization (electric dipole moment per unit area) of the electron or hole charge distribution is found by multiplying the dipole moment associated with $\mathbf{R}$ by the areal density of orbitals in a magnetic field [12], $|e|B/2\pi\hbar$; we obtain

$$\mathbf{P}^{e,h}(\mathbf{R},t) = \frac{|e|B}{2\pi\hbar}\int d^2\mathbf{r}_{e,h}\mathbf{r}_{e,h}\rho_{\mathbf{R}}^{e,h}(\mathbf{r}_{e,h},t). \tag{12}$$

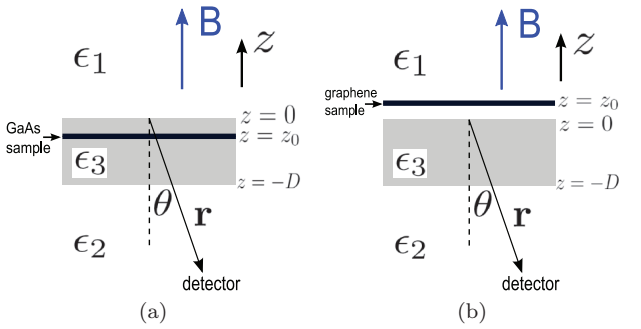

FIG. 2. (Color online) Experimental geometries for (a) GaAs and (b) graphene and bilayer graphene.

This expression will be used, along with the explicit forms of the envelope functions (see Refs. [7,8] and bilayer expressions in Sec. IV) to find the polarizations for the various systems we consider, along with the fields they radiate, in the next few sections.

It is possible to extend this approach and calculate the radiated fields resulting from the induced magnetic dipole moments and the induced electric quadrupole moment of the localized charged distributions $\rho_{\mathbf{R}}^{e,h}(\mathbf{r}_{e,h},t)$; we have done this, but for the systems and configurations considered here we found these contributions to be much smaller than those from the electric dipole moments, and so in the following we only present the radiation generated by the polarization (12).

III. RADIATED FIELDS

In this section, we present expressions for the fields radiated from sources in the experimental situations we consider. Figure 2 shows the configurations of interest. In Fig. 2(a), the source is a GaAs quantum well embedded in a slab of AlGaAs, for instance, which we take to have a dielectric constant ϵ_3. The surrounding materials, 1 and 2, will be taken as air. In Fig. 2(b), the source is monolayer or bilayer graphene, which is assumed to be in material 1 (air) on top of a substrate layer, for instance SiC (material 3); material 2 is air. In both geometries, we think of the exciting pulses as entering from material 1, and inducing a source polarization. The subsequent radiation from the source, after multiple reflections from the two interfaces, could be detected either on the same side as the laser source (reflection geometry) or on the other side (transmission geometry). Below we give general expressions for the radiation received at a detector in the transmission geometry, in terms of a general areal source polarization $\mathbf{P}(\mathbf{R},t)$.

We very generally write the terahertz electric field at a point $\mathbf{r}$ in the detector region ($z < -D$) as a superposition of plane waves propagating (or evanescent) in the $-z$ direction,

$$\mathbf{E}(\mathbf{r},t) = \int_0^\infty \frac{d\omega}{2\pi}\int\frac{d^2\kappa}{(2\pi)^2}\mathbf{E}(\boldsymbol{\kappa},\omega)e^{i(\boldsymbol{\kappa}\cdot\mathbf{R}-w_2z-\omega t)} + \text{c.c.}, \tag{13}$$

where $\boldsymbol{\kappa}$ is the in-plane component of a wave vector and $w_i(\boldsymbol{\kappa}) \equiv \sqrt{\epsilon_i\omega^2/c^2 - \kappa^2}$, with the convention $\text{Im}\sqrt{Z} \geqslant 0$ and, if $\text{Im}\sqrt{Z} = 0$, then $\text{Re}\sqrt{Z} \geqslant 0$. For the terahertz frequency range we consider we take the ϵ_i to be frequency-independent. The polarization vectors associated with upward (+) and

downward (−) propagating (or evanescent) waves in medium i are given by $\hat{\mathbf{s}}_{i\pm} = \hat{\boldsymbol{\kappa}} \times \hat{\mathbf{z}}$ and $\hat{\mathbf{p}}_{i\pm} = \hat{\mathbf{s}}_{i\pm} \times \hat{\mathbf{v}}_{i\pm}$, and $\boldsymbol{\nu}_{i\pm} \equiv \boldsymbol{\kappa} \pm w_i \hat{\mathbf{z}}$; in the detector region there are only downward waves [13].

Though we do not show the details, we can calculate $\mathbf{E}(\boldsymbol{\kappa},\omega)$ using a transfer matrix approach that includes the Fresnel coefficients for reflection and transmission at each interface [13]. These Fresnel coefficients for s- and p-polarized light are given by

$$t_{ij}^{s} = \frac{2w_i}{w_i + w_j}, \qquad t_{ij}^{p} = \frac{2\sqrt{\epsilon_i \epsilon_j}\, w_i}{w_i \epsilon_j + w_j \epsilon_i},$$
$$r_{ij}^{s} = \frac{w_i - w_j}{w_i + w_j}, \qquad r_{ij}^{p} = \frac{w_i \epsilon_j - w_j \epsilon_i}{w_i \epsilon_j + w_j \epsilon_i}. \tag{14}$$

Note that these are dependent on $\boldsymbol{\kappa}$ through the $w_{i,j}$. Assuming the source to be localized in the plane $z = z_0$, after calculating an expression for $\mathbf{E}(\boldsymbol{\kappa},\omega)$, placing this expression into (13), and taking the asymptotic far-field limit [13], we finally obtain, for the s and p components of the detected field, the following result for the GaAs geometry [Fig. 2(a)]:

$$E^{q}(\mathbf{r},t) = -\frac{t_{32}^{q}}{4\pi c^2 \epsilon_0 r} \frac{w_2(\bar{\boldsymbol{\kappa}})}{w_3(\bar{\boldsymbol{\kappa}})} \times \sum_{n=0}^{\infty} \int d^2R \Big[\left(r_{32}^{q} r_{31}^{q}\right)^n \hat{\mathbf{q}}_{3-} \cdot \ddot{\mathbf{P}}(\mathbf{R}, T_n) + r_{31}^{q} \left(r_{32}^{q} r_{31}^{q}\right)^n \hat{\mathbf{q}}_{3+} \cdot \ddot{\mathbf{P}}(\mathbf{R}, T_n') \Big] + \text{c.c.}, \tag{15}$$

where q stands for either s or p, $\hat{\mathbf{q}} = \hat{\mathbf{s}}$ or $\hat{\mathbf{p}}$; all Fresnel coefficients and polarization vectors here are evaluated at $\bar{\kappa}$, where $\bar{\kappa} \equiv \sqrt{\epsilon_2}\omega \sin\theta/c$, $\bar{\boldsymbol{\kappa}}/\bar{\kappa}$ points along the projection of $\hat{\mathbf{r}}$ in the xy plane, and θ is the angle between the detector position $\mathbf{r}$ and the $-z$ axis. In this expression, the first term in square brackets represents light that is initially emitted downward from the source, subsequently undergoing n pairs of reflections from the bottom and top interfaces before going to the detector. The second term represents light that is initially emitted upwards and undergoes a reflection from the top interface before undergoing n pairs of reflections from the bottom and top interfaces and then going to the detector. Owing to the different travel times of the light in going from the source to the detector, the second derivative of the source dipole moment is evaluated at retarded times T_n and T_n', where

$$T_n = t - W_3\left[(2n+1)D + z_0\right] + W_2 D + \sqrt{\epsilon_2}\frac{\hat{\mathbf{r}}\cdot\mathbf{R}}{c} - \sqrt{\epsilon_2}\frac{r}{c},$$
$$T_n' = t - W_3\left[(2n+1)D - z_0\right] + W_2 D + \sqrt{\epsilon_2}\frac{\hat{\mathbf{r}}\cdot\mathbf{R}}{c} - \sqrt{\epsilon_2}\frac{r}{c},$$

and we have defined $W_i \equiv w_i(\bar{\boldsymbol{\kappa}})/\omega$. For example, in the expression for T_n, the last term represents the retardation due to the travel from the system to the detector, the second last term represents the retardation or advancement that results from different parts of the source being at different distances from the detector at nonnormal detection angles, while other terms represent the travel time within the sample including the various reflections.

The same type of calculation can be performed for the radiation resulting from graphene monolayer and bilayer samples [Fig. 2(b)] with the detector in a transmission configuration. We find

$$E^{q}(\mathbf{r},t) = -\frac{t_{31}^{q} t_{32}^{q}}{4\pi c^2 \epsilon_0 r} \frac{w_2(\bar{\boldsymbol{\kappa}})}{w_1(\bar{\boldsymbol{\kappa}})} \sum_{n=0}^{\infty} \left(r_{31}^{q} r_{32}^{q}\right)^n \hat{\mathbf{q}}_{1-} \cdot \ddot{\mathbf{P}}(\mathbf{R}, T_n'') + \text{c.c.}, \tag{16}$$

where all Fresnel coefficients are, again, evaluated at $\bar{\boldsymbol{\kappa}}$, and the retarded times are given by

$$T_n'' = t - W_1 z_0 + W_2 D - (2n+1) W_3 D + \sqrt{\epsilon_2}\hat{\mathbf{r}}\cdot\mathbf{R}/c - \sqrt{\epsilon_2} r/c.$$

This can be interpreted physically in terms of the various reflections and transmissions on the way to the detector as before.

The fields presented above can be calculated once the form of the induced dipole moment distribution is known, according to the particular system under consideration; these will be specified in the next section.

IV. QUANTUM WELLS, GRAPHENE, AND BILAYER GRAPHENE

In previous work [7,8], we discussed the selection rules for one- and two-photon excitation processes in GaAs quantum wells and monolayer graphene in a magnetic field. These are summarized in Table I. In a quantum well, it was found that a time-dependent electron current could be induced through an interference between a one-photon transition, involving a photon at $2\omega_0$ traversing the band gap, and a two-photon transition, involving two photons at ω_0, which cause an electron to be excited from a given valence band state v to two different conduction band states c and c' (where c, v, and c' each label a set including a Landau level index, an index describing the quantum well confinement, and a spin index). As can be seen from the selection rules, the one- and two-photon processes place electrons in final

TABLE I. Selection rules for GaAs, monolayer graphene, and bilayer graphene in a magnetic field, for transitions from a valence band to a conduction band. For GaAs and monolayer graphene, the Landau indices for the conduction and valence bands are n and m respectively; for bilayer graphene, they are r_c and r_v, respectively. Bilayer conduction (valence) bands are labeled by I_c (I_v). In all cases, the spin index $s_c = s_v$, and for monolayer and bilayer graphene, the valley index $d_c = d_v$.

	GaAs	Graphene monolayer	Graphene bilayer
1-photon transition	$n = m$	$n = \lvert m\rvert \pm 1$	$I_c = C_1$ or C_2, $I_v = V_1$ or V_2 $r_c = r_v \pm 1$
2-photon transition	$n = m \pm 1$	$n = \lvert m\rvert \pm 2$	$I_c = C_1$ or C_2, $I_v = V_1$ or V_2 $r_c = r_v \pm 2$

states that differ by ± 1 in their Landau indices, with no difference in their spin indices. The electron current rotates counterclockwise at a frequency corresponding to the energy difference between these final Landau levels. Similarly, a hole current is produced which arises from an interference between one- and two-photon transitions putting an electron in the same conduction state c but originating from adjacent Landau levels in the valence band. This hole current rotates clockwise at a frequency corresponding to the energy difference between these two valence levels v and v'.

For the material polarization induced by the incident pulses, using (10), (11), (12) and the explicit expressions for the envelope functions [7], we find

$$\mathbf{P}^e(\mathbf{R},t) = \frac{e\beta}{2\pi}\begin{pmatrix}1\\ i\end{pmatrix}\sum_{cvc'} d_{cv}(\mathbf{R},t)d^*_{c'v}(\mathbf{R},t) \times (\sqrt{n}\delta_{n'+1,n} \pm \sqrt{n+1}\delta_{n',n+1})\delta_{n_w n'_w}\delta_{s_c s'_c} \quad (17)$$

for the electron contribution, and

$$\mathbf{P}^h(\mathbf{R},t) = -\frac{e\beta}{2\pi}\begin{pmatrix}1\\ i\end{pmatrix}\sum_{cvv'} d_{cv}(\mathbf{R},t)d^*_{cv'}(\mathbf{R},t) \times (\sqrt{m'}\delta_{m+1,m'} \pm \sqrt{m'+1}\delta_{m,m'+1})\delta_{m_w m'_w}\delta_{s_v s'_v} \quad (18)$$

for the hole contribution. Here, the upper (lower) signs and quantities in parentheses refer to the x (y) components. Also n and n' (m and m') are the Landau indices associated with the states c and c' (v and v'), respectively, n_w and n'_w (m_w and m'_w) are the well quantum numbers, s_c and s'_c (s_v and s'_v) are the spin indices, and $\beta = \sqrt{|e|B/2\hbar}$.

We see from the above that, analogous to the current density, the electron contribution to the source polarization consists of a sum of terms involving interference of two transitions connecting the same initial state v with two final states c and c' differing by 1 in their Landau indices, while in the hole contribution, each term involves an interference of two transitions connecting two initial states v and v', differing by 1 in their Landau indices, with the same final state c. In both cases, the dipole moment vector rotates in the plane counterclockwise (in the case of electrons) or clockwise (in the case of holes) at a frequency equal to the spacing between the two final states (in the case of electrons) or the two initial states (in the case of holes). It should be pointed out that since the Landau level spacing in GaAs in each band is constant—a result of the parabolic band structure—each term in the summation oscillates with the same frequency, so there is only one overall rotation frequency for the electron contribution and one overall frequency for the hole contribution.

A similar analysis can be performed for a graphene monolayer. In this case, the states in the conduction and valence bands are labeled by a Landau level index ($n > 0$ for conduction states, $m < 0$ for valence states), a spin index s, and a valley index d. The polarization and current density for graphene can be calculated the same way as for GaAs, using the expressions for the envelope functions presented in our previous work [8]. The result for the polarization is

$$\mathbf{P}^e(\mathbf{R},t) = \frac{e\beta}{4\pi}\begin{pmatrix}1\\ i\end{pmatrix}\sum_{cvc'} d_{cv}(\mathbf{R},t)d^*_{c'v}(\mathbf{R},t)[(\sqrt{n'}+\sqrt{n'+1}) \times \delta_{n',n-1} \pm (\sqrt{n}+\sqrt{n+1})\delta_{n'-1,n}]\delta_{s_c s'_c}\delta_{d_c d'_c} \quad (19)$$

for the electron contribution, and

$$\mathbf{P}^h(\mathbf{R},t) = -\frac{e\beta}{4\pi}\begin{pmatrix}1\\ i\end{pmatrix}\sum_{cvv'} d_{cv}(\mathbf{R},t)d^*_{cv'}(\mathbf{R},t) \times [(\sqrt{|m|}+\sqrt{|m|+1})\delta_{|m|,|m'|-1} \pm (\sqrt{|m'|}+\sqrt{|m'|+1})\delta_{|m|-1,|m'|}]\delta_{s_v s'_v}\delta_{d_v d'_v} \quad (20)$$

for the hole contribution. Similar expressions were found for the current density [8].

As in the case of GaAs, it can be seen from these expressions and the selection rules in Table I that the polarization and current result from interferences between one- and two-photon processes sharing an initial state but having adjacent final states (electron contribution), or sharing a final state but having adjacent initial states (hole contribution). Each term again rotates at a frequency corresponding to the energy difference between the two final or initial states; but since the Landau levels in graphene are not evenly spaced—a result of the linear dispersion which leads to energy levels proportional to the square root of the Landau index in a magnetic field [8]—several different frequencies will contribute.

Furthermore, for linearly polarized incident light, for each term in the summation in the electron contribution there is a corresponding term in the hole contribution which is equal in magnitude, due to the symmetric band structure of graphene, but rotating in the opposite direction. Thus the overall material polarization will simply oscillate along one particular direction, which depends on the polarization directions of the exciting pulses.

The calculations previously performed for GaAs quantum wells and monolayer graphene can be extended to the case of a graphene bilayer; this calculation will be outlined here. The Hamiltonian for Bernal-stacked bilayer graphene in a magnetic field can be obtained by applying minimal coupling to the 4×4 envelope function Hamiltonian for a bilayer in the absence of a magnetic field [14], which yields

$$H = \begin{pmatrix} 0 & 0 & 0 & v_F\pi_- \\ 0 & 0 & v_F\pi_+ & 0 \\ 0 & v_F\pi_- & 0 & \gamma_1 \\ v_F\pi_+ & 0 & \gamma_1 & 0 \end{pmatrix}, \quad (21)$$

where v_F is the Fermi velocity for a monolayer, γ_1 is the coupling constant between the two sheets, and $\pi_\pm \equiv [(\hbar/i)\nabla_x - eA^B_x] \pm [(\hbar/i)\nabla_y - eA^B_y]$; $\mathbf{A}^B$ is the vector potential describing the magnetic field in the symmetric gauge. The four components of the Hamiltonian refer to, in order, the A sublattice of the upper sheet, the B sublattice of the lower sheet, the A sublattice of the lower sheet, and the B sublattice of the upper sheet [14]. Ignoring for now the coupling γ_1, the

eigenstates of the system can be written as

$$\bar{\Psi}_{nlS} = Q_n \begin{pmatrix} -\delta_{S,1}\mathrm{sgn}(n) i \phi_{|n|-1,l} \\ \delta_{S,2}\phi_{|n|,l} \\ -\delta_{S,2}\mathrm{sgn}(n) i \phi_{|n|-1,l} \\ \delta_{S,1}\phi_{|n|,l} \end{pmatrix}, \tag{22}$$

where $\phi_{|n|,l}$ is the wave function for a two-dimensional electron in a magnetic field with $|n|$ and l representing the right- and left-circular quantum numbers, respectively, $Q_n = 1/\sqrt{2}$ for $n \neq 0$ and 1 for $n = 0$, and $S = 1$ ($S = 2$) refers to states on the upper (lower) sheet. To determine the eigenstates, accounting for the coupling between the sheets, we perform a numerical calculation using an expansion in terms of the above uncoupled eigenstates:

$$\Psi_{Ir,l} = \sum_{n,S} a_{nS}^{Ir,l} \bar{\Psi}_{nlS}. \tag{23}$$

Note that the Hamiltonian does not couple states of different l. The new states are characterized by quantum numbers I and r which are explained below. The numerical calculation shows that there are two degenerate states at zero energy, and that the energy spectrum is symmetric about the zero energy, as it is for monolayer graphene. For monolayer graphene, we found that Landau states in a particular band (conduction or valence) have a nonzero velocity matrix element only with states with adjacent Landau indices. Motivated by this fact, we can construct a chain of states for the bilayer, starting from one of the zero-energy states, with each subsequent addition to the chain being the state that is the closest in energy to the previous state and connected to it by a nonzero matrix element of the velocity operator $\hat{\mathbf{v}} = \partial H/\partial \hat{\mathbf{p}}$.

Working in this manner, we find that the states fall into four such chains or sets of states, which correspond to the four bands that are present in the absence of a magnetic field. These sets are shown schematically in Fig. 3. The states can then be characterized by the quantum numbers I and r, where I labels one of the four bands (valence bands V_1 and V_2, and conduction bands C_1 and C_2), while r labels the states within each band, starting from $r = 1$. All of these states are degenerate in l, and the velocity operator does not connect states of different l. Further, we find that any level has a nonzero velocity matrix element with a level in any of the four bands which has its r value differing from it by ± 1, while it has a zero matrix element with all other states, including itself.

From these properties of the velocity matrix elements, we can deduce the allowed optical transitions from (5), (6), (7), (8), and (9). These selection rules are summarized in Table I. From (5) and (6), which contain one velocity matrix element, we see that a one-photon transition can occur from any valence band to any conduction band, changing the value of r by ± 1. On the other hand, the second-order coefficient contains terms that have two velocity matrix elements [see (7) and (8)], representing a transition from a valence state v to a conduction state c through an intermediate conduction or valence state c' or v'. Thus a two-photon transition can occur from any valence band to any conduction band, changing the value of r by ± 1 twice, so that the overall change in r is ± 2. [The two-photon processes by which r changes by 0 are disallowed as the two terms in (7), and the first pair of terms as well as the last pair of terms in (8)—the virtual electron and virtual hole terms—cancel.] Note that this is similar to the situation in monolayer graphene, except for the presence of four bands instead of two.

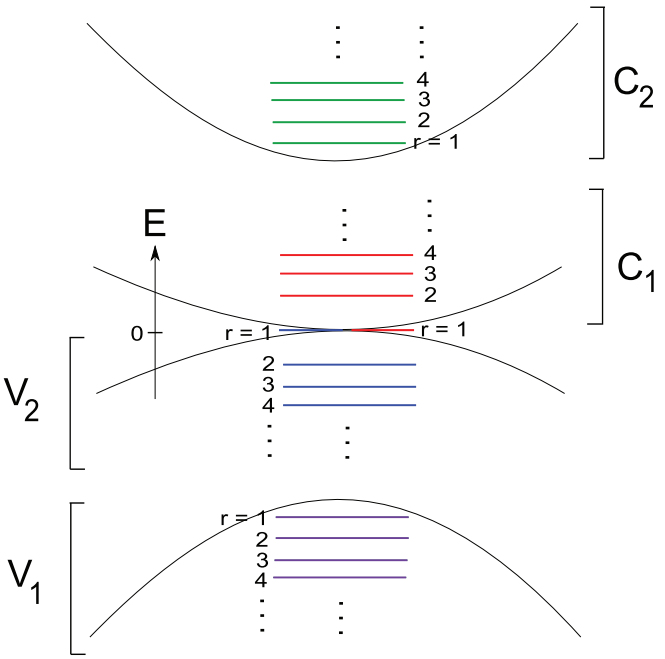

FIG. 3. (Color online) Schematic of energy levels of bilayer graphene.

The behavior of the induced current density can be deduced from a consideration of these allowed transitions. Just as we found for GaAs and monolayer graphene, a counterclockwise-rotating electron current results from the interference of one- and two-photon transitions from a state in the valence band to states in the conduction band whose r values differ by ± 1 (electron current). Meanwhile a clockwise-rotating hole current results from interference between transitions to a conduction state from valence states whose r values differ by ± 1. In principle, the two final states in the electron current, or the two initial states in the hole current, do not have to be in the same band. However, if they are in different conduction bands, or different valence bands, the current rotation frequency will be at least 30 times greater than that which results from their being in the same band, and we will therefore not focus on the former situation in our results.

In Fig. 4 we present polar plots of the total current, including both the electron and hole contributions, as a function of the polarization angle between the linear polarization directions of the incident pulses, at time $t = 0$ corresponding to the time when the pulses have their peak intensity. For the purpose of comparison to the case of no magnetic field treated by Rioux *et al.* [14], we adopt their classification of the two-photon processes into four types, distinguished by the initial, intermediate, and final bands involved in the transition. This classification is presented in Table II. Separate plots are made in Fig. 4 for the current contributions resulting from each of the four classes of two-photon transition. We note that our results for $t = 0$ for the 2BT, 3BT, and SOT match the shape

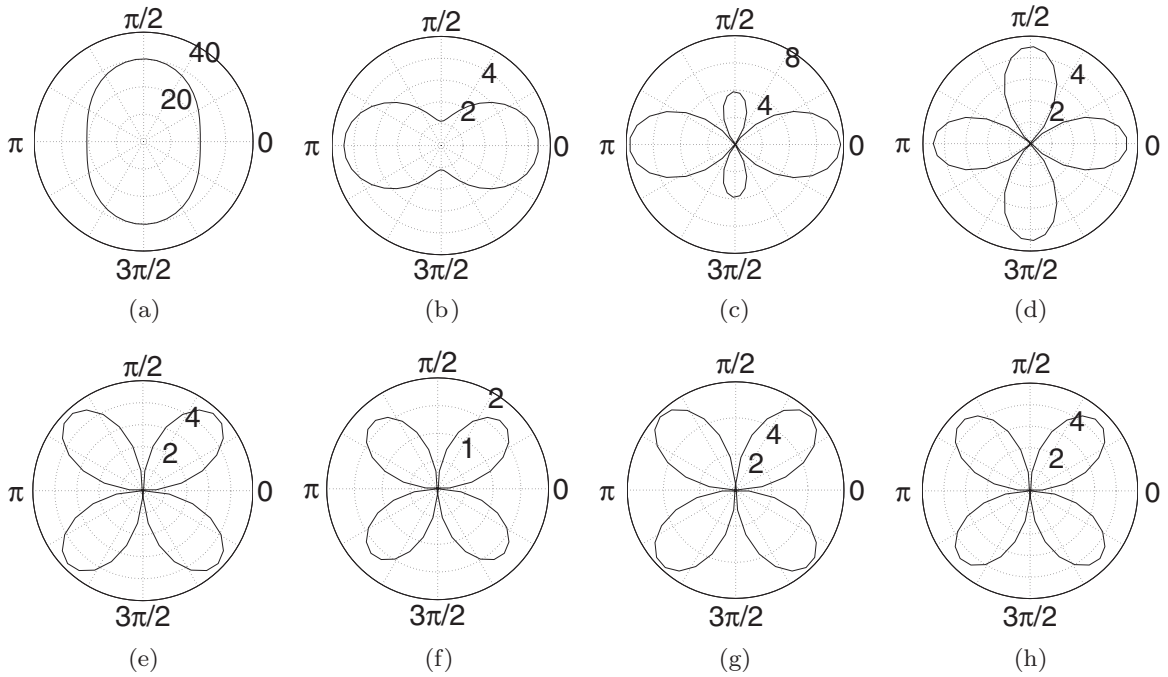

FIG. 4. Injected current density (in A/m) vs relative polarization angle for GLT [(a) and (e)], 2BT [(b) and (f)], 3BT [(c) and (g)], and SOT [(d) and (h)]. Top row shows x components, bottom row shows y components. The angle is measured from the $2\omega_0$-pulse polarization direction (here assumed to be the $+x$ direction) to the ω_0-pulse polarization direction. The experimental parameters are identical to those given in Sec. V for the bilayer, but with the pulse frequencies doubled and infinite scattering time.

of the corresponding plots found in Rioux *et al.* Of course, as time goes by, the current oscillates with various frequency components corresponding to the different pairs of transitions that are excited, whereas the current is static in the absence of a magnetic field. Again, the nonparabolicity of the band structure leads to Landau levels that are not equally spaced, and therefore to currents that have multiple frequency components.

A difference, however, is found in the shape of the plot for the GLT compared to that in the absence of a magnetic field. The GLT in the paper of Rioux *et al.* was of the same shape as that of the SOT, which had the same shape as the SOT in Fig. 4. This difference arises because the authors of the above paper account only for the current arising from interference between absorption of one photon at $2\omega_0$ [represented by (5)] and absorption of two photons at ω_0 [represented by (7)]. It did not include the current that arises from the other interference process, that which involves a one-photon process where a photon at ω_0 is absorbed [represented by (6)], along with a two-photon process where a photon at $2\omega_0$ is absorbed and a photon at ω_0 is emitted [represented by (8)] [15]. In the latter interference mechanism, the one-photon process excites an electron from V_2 to C_1 directly, while the two-photon process excites an electron from V_2 to C_1 through an intermediate state in V_1 or C_2. Since the photon energies we used in these plots are large enough to connect band V_2 to C_2, or band V_1 to C_1, with a $2\omega_0$ photon, the two-photon process is greatly enhanced compared to what it would be otherwise, as the transition to or from the intermediate state is near resonance with one of the photon frequencies. Normally, in monolayer graphene, this particular interference process would not be as significant in magnitude because there is no intermediate state such that a transition to or from this state would be near resonance. In addition to the presence of 2BT, 3BT, and SOT contributions, this constitutes a notable qualitative difference between the behavior of a bilayer and that of a monolayer.

TABLE II. Classification of two-photon transitions of bilayer graphene in a magnetic field into four types distinguished by the combination of initial band, intermediate band, and final band. The four types are the gapless term (GLT), the 2-band term (2BT), the 3-band term (3BT), and the split-off term (SOT).

	Initial band	Intermediate band	Final band
GLT	V_2	V_1, V_2, C_1, C_2	C_1
2BT	V_1	V_1, C_1	C_1
	V_2	V_2, C_2	C_2
3BT	V_1	V_2, C_2	C_1
	V_2	V_1, C_1	C_2
SOT	V_1	V_1, V_2, C_1, C_2	C_2

To conclude this section, we mention the material polarization induced in the bilayer. This is calculated using (10), (11), (12), and the eigenfunction (23). It is found that the behavior of the polarization can qualitatively be described similarly to that of the current density, as a superposition of rotating electron and hole contributions resulting from interfering one- and two-photon transitions. This is as one would expect from the classical expression $\mathbf{J} = d\mathbf{P}/dt$.

V. NUMERICAL RESULTS

In this section we present results for the fields at the detector that result from the induced charges and currents. Note first that

the electric field amplitudes in (1) and appearing in subsequent formulas refer to the electric field from the applied pulses experienced at the position of the sample. To relate this to the field incident on the structure, which is experimentally controllable, one can perform an analysis similar to that in Sec. III, accounting for the various transmissions and reflections of the incident light. These will cause a Gaussian (in time) incident pulse to become non-Gaussian at the sample, since the pulses will reach the sample multiple times. For simplicity, we assume that $z_0 = 0$ for graphene, and the GaAs QW is so close to the upper interface, that for both structures the induced polarization will decay by the time a reflected wave reaches the sample. For the structures and pulse lengths we assume below, this holds, and ensures that the reflected fields from the lower interface do not come into play during the time window in which we are interested; thus the field at the sample can be considered Gaussian and our formulas are valid. The field at the sample is then equal to the incident field multiplied by $t_{13}(\boldsymbol{\kappa} = 0)$ for GaAs and $[1 - r_{31}(\boldsymbol{\kappa} = 0)]$ for graphene. The calculation can be performed for the more general case, but the formulas in Sec. II become more complicated. The intensities quoted in what follows refer to the light incident on the structure.

In calculating the radiated fields, we have also neglected the radiation reaction, or the decay of induced charges and loss of energy due to the radiation [16]. The time scale for this decay is estimated to be much longer than the relevant timescale we consider here, so our neglect is justified.

For the case of a GaAs quantum well, we take the incident ω_0 pulse from region 1 to have a duration of 150 fs FWHM with a peak intensity of 200 GW/cm^2, and the $2\omega_0$ pulse to have a duration of 106 fs with a peak intensity of 200 MW/cm^2; the pulse durations are related by a factor of $\sqrt{2}$ as would occur when the second harmonic pulse is derived from the fundamental using a doubling crystal, as is the usual practice; and the intensities are selected to be low enough that our perturbative treatment of the optical field is valid. We choose $\hbar\omega_0 = 878$ meV, the same value as adopted earlier [7], chosen such that the ω_0 pulse is insufficient to cross the band gap but the $2\omega_0$ pulse can. In the 2-band effective mass model that we are using [7], the $2\omega_0$-pulse energy should be less than about 2 eV to avoid connecting other bands; the pulse energies we have chosen satisfy this condition. The relative phase parameter of the pulses is chosen to be $\Delta\varphi \equiv 2\varphi_{\omega_0} - \varphi_{2\omega_0} = \pi/2$ to maximize the induced current. The thickness of the sample in which the quantum well is embedded (medium 3) is assumed to be $D = 400$ μm with a dielectric constant $\epsilon_3 = 12$. As in earlier experimental work [10], we choose $R_1 = R_2 = 9$ μm. The detector is taken to be at a distance of 10 cm below the sample detecting at an angle of $\theta = 0$.

The two components of the detected electric field can be calculated using (15), (17), and (18). These are plotted in Fig. 5 as Lissajous figures to show the polarization of the emitted light, for the case of applied pulses collinearly polarized in the $+x$ direction. It can be seen that the field from the electron contribution [Fig. 5(a)], after an initial buildup during the period that the exciting pulses are at play, is circularly polarized. This is to be expected considering that the electrons in the sample undergo cyclotron motion, at a

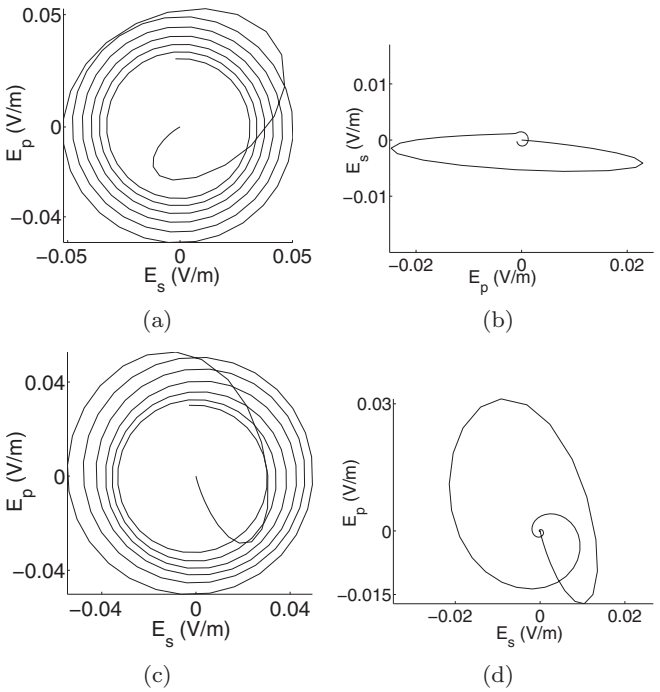

FIG. 5. Lissajous figures for GaAs with collinear incident pulses. For $\tau = 5$ ps, we plot the (a) electron contribution, (b) hole contribution, and (c) total contribution; (d) shows the total contribution for $\tau = 200$ fs. The time T, measured at the sample, runs from -200 fs to 1.5 ps, where $T = 0$ corresponds to the peak incident intensity at the sample. See text for pulse parameters.

frequency corresponding to the Landau level spacing in the conduction band, which is also the frequency of oscillation of the detected field. Similar considerations apply for the hole contribution to the current, shown in Fig. 5(b). The period during which the applied pulse is passing through the sample manifests itself as the large swing to the right and back to the left. After the pulse passes, the holes start to undergo cyclotron motion in the direction opposite to the electrons, and this is indicated by the smaller circular region in Fig. 5(b), rotating in the direction opposite to that in Fig. 5(a). Additional physical insight into the nature of these curves can be obtained by considering the behavior of the charges in the sample. As we showed in our previous work [7], the hole charge density around any point in the plane at $t = 0$ is localized toward the $+y$ direction of the point, and so the initial buildup of the dipole moment occurs along the y direction. Keeping in mind that s polarization corresponds to the $-y$ direction for normal detection angle while p polarization corresponds to the $+x$ direction, as well as the fact that the cyclotron period for hole motion is large compared to the time scale of the initial buildup, this means that the primary contribution to the emitted field should be polarized along the s direction. Then, after the initial stage, we should see a circularly polarized field with an amplitude that is small compared to the field of the initial stage, due to the comparatively slow rotation of the holes. This is indeed the behavior that is observed in Fig. 5(b). Similar physical considerations apply to Fig. 5(a); the differences in its appearance compared to Fig. 5(b) are due to the fact that

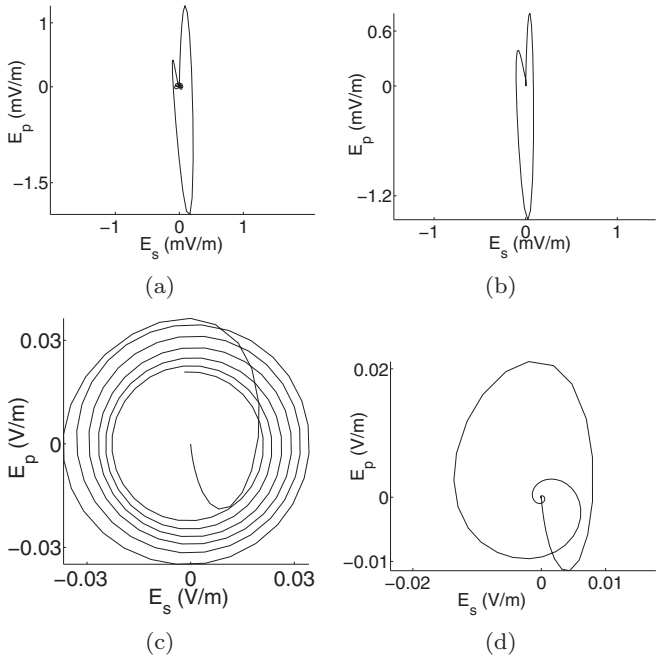

FIG. 6. Lissajous figures for GaAs for total (electron + hole) field for (a) cross-linear polarization $\tau = 5$ ps; (b) cross-linear polarization and $\tau = 200$ fs; (c) co-circular polarization and $\tau = 5$ ps; (d) co-circular polarization and $\tau = 200$ fs. The time T, measured at the sample, runs from -200 fs to 1.5 ps, where $T = 0$ corresponds to the peak incident intensity at the sample. See text for pulse parameters.

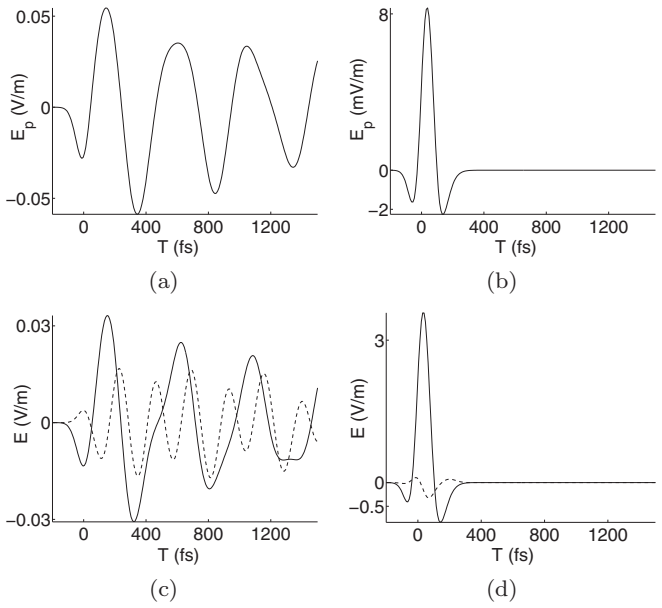

FIG. 7. Total field vs time for monolayer graphene for (a) collinear polarization, $\tau = 5$ ps; (b) collinear polarization, $\tau = 50$ fs; (c) co-circular polarization, $\tau = 5$ ps; (d) co-circular polarization, $\tau = 50$ fs. Solid line represents the p component and dashed line represents the s component. The time T is measured at the sample, where $T = 0$ corresponds to the peak incident intensity at the sample. See text for pulse parameters.

the time scale for electron cyclotron rotation is comparable to that of the exciting pulses, and therefore the amplitudes during each stage are comparable.

In Fig. 5(c), we plot the sum of the electron and hole contributions. As described above, the behavior after the exciting pulses have passed is dominated by the electron contribution. In all of the above plots, we have assumed a long scattering time of 5 ps for all of the τ_{cv} in order to illustrate the cyclotron behavior. Figure 5(d) shows the sum of the electron and hole contributions with a more realistic scattering time [17] of $\tau = 200$ fs. As we expect, the field builds up and then undergoes circular motion while decaying rapidly.

Figures 6(a) and 6(b) display the fields for the case of cross-linear polarization, plotted against time, for the long and short scattering times. The ω_0 pulse is taken to be polarized along the $+x$ direction and the $2\omega_0$ pulse along the $+y$ direction. As before, there is an initial stage where the applied pulses are passing through the sample, corresponding to the large variation along the E_p direction, followed by a stage of cyclotron motion, corresponding to the smaller loops in the plot. The large variation in the E_p direction is mainly caused by the buildup of hole density and dipole moment along the x direction, which corresponds to the p direction, before the cyclotron motion gets going.

The fields are plotted for the case of co-circular polarization in Figs. 6(c) and 6(d) for long and short scattering times, respectively, where both incident pulses are σ_+-polarized. The plots are similar to those for collinear polarization, as similar charge distributions are induced in the sample. Indeed, the collinear case can be considered to be a combination of the case of co-circular σ_+ polarization and the case of co-circular σ_- polarization. Finally, we emphasize that for all types of polarization, we obtain circularly polarized light at the detector, since electrons and holes will always move in cyclotron orbits in a magnetic field. For GaAs quantum wells we will obtain two light frequencies corresponding to the cyclotron frequencies of electrons and holes.

Next we look at the results for graphene monolayers and bilayers. For both cases, following earlier work [8,10], we choose $\hbar\omega_0 = 259$ meV and we take the applied ω_0 pulse to have a duration of 220 fs FWHM with a peak intensity of 50 MW/cm^2, and the $2\omega_0$ pulse to have a duration of 156 fs with a peak intensity of 1 MW/cm^2; the intensities are again chosen such that the perturbative treatment is valid. For both the monolayer and bilayer, the pulse energy should be less than about 2 eV to stay within the linear regime [8] (for monolayer graphene) or within the regime of validity of our tight-binding Hamiltonian [14] (for bilayer graphene); our chosen pulse energies satisfy this condition. The relative phase parameter is $\Delta\varphi = \pi/2$ as before. The substrate is assumed to be SiC with a dielectric constant $\epsilon_3 = 6.8$ and thickness $D = 400$ μm. We take $R_1 = R_2 = 9$ μm, and the detector is again at a distance of 10 cm below the sample at $\theta = 0$.

For monolayer graphene, the components of the detected field are calculated using (16), (19), and (20). Plots of the field are given in Fig. 7 for collinearly polarized incident pulses [Figs. 7(a) and 7(b)] for long (5 ps) and short [18] (50 fs) scattering times, as well as for co-circularly polarized σ_+ incident pulses [Figs. 7(c) and 7(d)]. Looking first at the results for collinear polarization, we find that the s component of the detected field is zero, and that the p component, shown

in Fig. 7(a), is nonzero. This is to be expected because, as mentioned in the previous section, the symmetric band structure of graphene ensures that the electron and hole contributions to the current density are equal in magnitude but rotate in opposite directions, resulting in an overall current—and therefore emitted field—oscillating along one direction, the x direction. From (19) and (20) we see that the electron dipole moment is composed of terms each involving two transitions, from a particular valence state to two conduction states, while the hole dipole moment is also composed of terms each involving two transitions, from two valence states to a particular conduction state. Due to the symmetric band structure, the term in the electron dipole moment involving, for example, the transitions $-15 \rightarrow 16$ and $-15 \rightarrow 17$ will have the same magnitude as the term in the hole dipole moment involving the transitions $-16 \rightarrow 15$ and $-17 \rightarrow 15$. These electron and hole contributions will therefore cancel in one direction, since they are equal in magnitude but oppositely rotating.

In Fig. 7(c) we show a similar plot for co-circular polarization, including both the s and p components. Note in this case that both the s and p components are nonzero, unlike in the case of collinear polarization. This can be understood by looking at the various transitions involved in the dipole moments. In the example above, the transitions in the hole dipole moment, $-16 \rightarrow 15$ and $-17 \rightarrow 15$, are required in order to cancel one component of the corresponding electron contribution. However, these transitions cannot be excited by σ_+-polarized light because σ_+-polarized light can only increase the absolute value of the quantum number in a transition, and thus the cancellation does not occur. The cancellation is present for linearly polarized incident light because it contains a σ_--polarized component that can excite these transitions. Also, it should be mentioned that multiple frequencies of oscillation contribute to the plots, since the Landau level spacings are not all the same, as they are in GaAs.

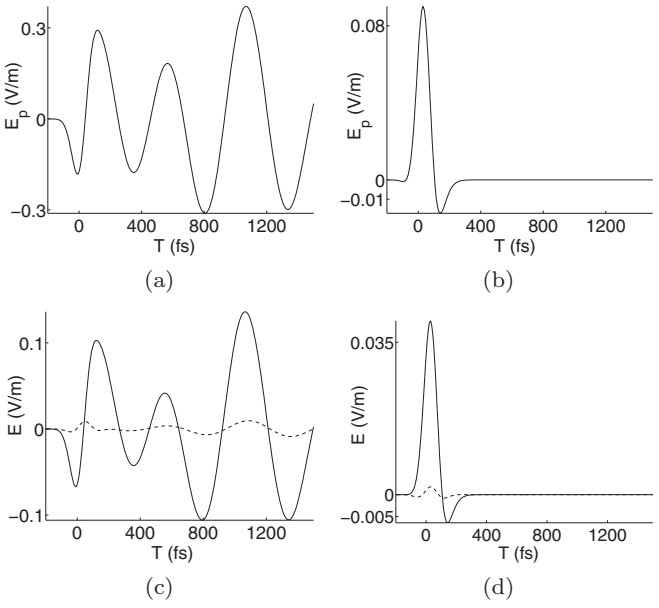

FIG. 8. Total field vs time for bilayer graphene for (a) collinear polarization, $\tau = 5$ ps; (b) collinear polarization, $\tau = 50$ fs; (c) co-circular polarization, $\tau = 5$ ps; (d) co-circular polarization, $\tau = 50$ fs. Solid line represents the p component and dashed line represents the s component. The time T is measured at the sample, where $T = 0$ corresponds to the peak incident intensity at the sample. See text for pulse parameters.

Finally, Fig. 8 shows the same plots for bilayer graphene. As for monolayer graphene, the s component cancels for collinear polarization, while both components survive for co-circular polarization. The reasons are the same as for monolayer graphene: the symmetric band structure along with the different selectivity of transitions of σ_+ and σ_- light. The main differences between the plots for monolayer graphene and bilayer graphene are due to the presence of different frequencies of oscillation as determined by the bilayer Landau level structure, as well as the additional complexities resulting from the presence of four bands instead of two.

Finally, we mention that the electric field magnitudes predicted from our calculations are comparable to those predicted in the absence of a magnetic field; the latter have been detected in similar coherent control experiments [9,10]. Thus it is expected that the effects outlined here should also be experimentally observable.

VI. CONCLUSION

In this paper we have calculated the time-dependent terahertz signal emitted by coherently injected photocurrents in the presence of a magnetic field. We have looked in detail at the predictions for a GaAs quantum well, monolayer graphene, and Bernal-stacked bilayer graphene. In a GaAs sample, it was found that circularly polarized radiation is emitted, corresponding to electrons and holes executing cyclotron motion after injection. Similar results are found in graphene and bilayer graphene, but with the presence of multiple frequencies, and linearly polarized radiation when the incident beams are collinear, which results from the symmetrical band structure in these systems. For each system, the particular frequencies excited reflect the underlying dispersion relation of the structure. In all cases, we have accounted for the finite beam size and shape, and for decay processes in a phenomenological manner, and so we expect the experimentally obtained terahertz radiation pattern to be similar to what we have presented here. A more detailed calculation would account more rigorously for the different kinds of scattering and decay processes, but for our purposes, a phenomenological treatment is sufficient. We emphasize that our predictions show a rich behavior strongly dependent on the phenomenological times introduced, and thus from experimental results one should be able to approximately extract the phenomenological time, as well as see evidence for the necessity of extending the simple theory presented here for transport in these structures. The terahertz radiation that we have calculated here should be detectable by these experiments.

We have also calculated numerically the current injected in a graphene bilayer sample and compared it with that previously obtained for a monolayer. In particular, it was found that the presence of two additional bands, as well as an additional interference process—that between a one-photon process of absorption at ω_0 and a two-photon process of absorption at

$2\omega_0$ and emission at ω_0—can significantly alter the qualitative behavior of bilayer graphene compared to monolayer graphene. This can be seen especially in the dependence of the current on the relative polarization angle of the two incident beams, and should be detectable experimentally. As in the example of monolayer and bilayer graphene in the absence of a magnetic field, experiments in the presence of a magnetic field should be able to distinguish between these two versions of graphene. They should also provide an important probe of transport in these structures, and more generally how it is different in different versions of graphene.

ACKNOWLEDGMENTS

This work was supported by the Natural Sciences and Engineering Research Council (NSERC) of Canada, in part through a CGS-M to K.M.R.

[1] N. S. Ginsberg, S. R. Garner, and L. V. Hau, Nature (London) **445**, 623 (2007).
[2] L. Zhu, V. Kleiman, X. Li, S. P. Lu, K. Trentelman, and R. J. Gordon, Science **270**, 77 (1995).
[3] M. J. Stevens, R. D. R. Bhat, J. E. Sipe, H. M. van Driel, and A. L. Smirl, Phys. Status Solidi B **238**, 568 (2003).
[4] H. M. van Driel and J. E. Sipe, in *Ultrafast Phenomena in Semiconductors*, edited by K. T. Tsen (Springer-Verlag, New York, 2001), pp. 261–306.
[5] R. D. R. Bhat and J. E. Sipe, Phys. Rev. Lett. **85**, 5432 (2000).
[6] A. Najmaie, R. D. R. Bhat, and J. E. Sipe, Phys. Rev. B **68**, 165348 (2003).
[7] K. M. Rao and J. E. Sipe, Phys. Rev. B **84**, 205313 (2011).
[8] K. M. Rao and J. E. Sipe, Phys. Rev. B **86**, 115427 (2012).
[9] H. M. van Driel, J. E. Sipe, and A. L. Smirl, Phys. Status Solidi B **243**, 2278 (2006).
[10] D. Sun, C. Divin, J. Rioux, J. E. Sipe, C. Berger, W. A. de Heer, P. N. First, and T. B. Norris, Nano Lett. **10**, 1293 (2010).
[11] C. Cohen-Tannoudji, B. Diu, and F. Laloe, *Quantum Mechanics*, Vol. 1 (Wiley, New York, 2006).
[12] Z. F. Ezawa, *Quantum Hall Effects: Field Theoretical Approach and Related Topics* (World Scientific, Singapore, 2000).
[13] D. Côté, J. E. Sipe, and H. M. van Driel, J. Opt. Soc. Am. B **20**, 1374 (2003).
[14] J. Rioux, G. Burkard, and J. E. Sipe, Phys. Rev. B **83**, 195406 (2011).
[15] J. Rioux, J. E. Sipe, and G. Burkard, presented at the APS March Meeting on March 3, 2014, in Denver, CO, USA.
[16] J. D. Jackson, *Classical Electrodynamics*, 3rd ed. (Wiley, New York, 1998).
[17] F. F. Fang, T. P. Smith III, and S. L. Wright, Surf. Sci. **196**, 310 (1988).
[18] Z. Jiang, E. A. Henriksen, L. C. Tung, Y.-J. Wang, M. E. Schwartz, M. Y. Han, P. Kim, and H. L. Stormer, Phys. Rev. Lett. **98**, 197403 (2007).